

arXiv:2307.11524v1 [cond-mat.mtrl-sci] 21 Jul 2023

Magnetic Proximity induced efficient charge-to-spin conversion in large area $\text{PtSe}_2/\text{Ni}_{80}\text{Fe}_{20}$ heterostructures

Richa Mudgal,[†] Alka Jakhar,[‡] Pankhuri Gupta,[†] Ram Singh Yadav,[†] B.
Biswal,^{¶,§} P. Sahu,^{¶,||} Himanshu Bangar,[†] Akash Kumar,^{†,⊥} Niru
Chowdhury,[†] Biswarup Satpati,[#] B. R. K. Nanda,^{¶,§} S. Satpathy,^{¶,||,§}
Samaresh Das,[‡] and P. K. Muduli^{*,†}

[†]*Department of Physics, Indian Institute of Technology Delhi, Hauz Khas, New Delhi-110016,
India*

[‡]*Center for Applied Research in Electronics, Indian Institute of Technology Delhi, Hauz Khas,
New Delhi-110016, India*

[¶]*Condensed Matter Theory and Computational Lab, Department of Physics, Indian Institute of
Technology Madras, Chennai 600036, India*

[§]*Center for Atomistic Modelling and Materials Design, Indian Institute of Technology Madras,
Chennai 600036, India*

^{||}*Department of Physics & Astronomy, University of Missouri, Columbia, MO 65211, USA*

[⊥]*Department of Physics, University of Gothenburg, Gothenburg-412 96, Sweden*

[#]*Surface Physics & Material Science Division, Saha Institute of Nuclear Physics, A CI of Homi
Bhabha National Institute, 1/AF Bidhannagar, Kolkata 700064, India*

E-mail: muduli@physics.iitd.ac.in

Abstract

As a topological Dirac semimetal with controllable spin-orbit coupling and conductivity, PtSe₂, a transition-metal dichalcogenide, is a promising material for several applications from optoelectric to sensors. However, its potential for spintronics applications is yet to be explored. In this work, we demonstrate that PtSe₂/Ni₈₀Fe₂₀ heterostructure can generate a large damping-like current-induced spin-orbit torques (SOT), despite the absence of spin-splitting in bulk PtSe₂. The efficiency of charge-to-spin conversion is found to be $(-0.1 \pm 0.02) \text{ nm}^{-1}$ in PtSe₂/Ni₈₀Fe₂₀, which is three times that of the control sample, Ni₈₀Fe₂₀/Pt. Our band structure calculations show that the SOT due to the PtSe₂ arises from an unexpectedly large spin splitting in the interfacial region of PtSe₂ introduced by the proximity magnetic field of the Ni₈₀Fe₂₀ layer. Our results open up the possibilities of using large-area PtSe₂ for energy-efficient nanoscale devices by utilizing the proximity-induced SOT.

The next generation of spintronic memories can be realized using spin-orbit torques (SOT), an energy-efficient and faster way to manipulate magnetization.¹ In ferromagnet (FM)/heavy metal (HM) bilayers, SOT describes the current-induced torque exerted on the FM layer. The flow of a charge current in an FM/HM system can generate a spin current, transverse to the direction of charge current flow, by mechanisms such as the spin Hall effect,² or Rashba-Edelstein.³ Typically heavy metals, such as Pt,^{4,5} W,⁵⁻⁷ and Ta^{8,9} are used to generate spin currents. Significant efforts have been reported to improve the energy efficiency of HM-based SOT devices.¹⁰⁻¹² One method to achieve a higher SOT efficiency is by replacing the HM layer with alternative materials that have large charge-to-spin conversion efficiency and high conductivity. Transition metal dichalcogenides (TMDs) are potential replacements of HM due to various properties such as tunable conductivity,^{13,14} high spin-orbit coupling,¹⁵⁻¹⁷ the presence of Dzyaloshinskii Moriya-interaction,¹⁸ tunable band structure,^{19,20} spin-layer locking²¹ and long spin-life time.²² The use of TMDs in SOT devices has shown a number of advantages, *e.g.*, the ability to control SOT using the crystal symmetry²³⁻²⁵ and electric field.²⁶

The Pt-based TMDs offer advantages such as high air stability,²⁷ and large spin-orbit coupling.²⁸ However, SOT studies on Pt-based TMDs have been limited to PtTe₂ for which a recent work showed

a large damping-like torque and SOT switching.²⁹ PtSe₂ is another Pt-based TMD offering high and tunable spin-orbit coupling.²⁸ It is also a type-II Dirac semi-metal, offering several topologically protected phenomena potentially useful for spintronic applications.³⁰ In addition, the band structure of PtSe₂ exhibits topological surface states,³¹ which can be exploited for topological spintronic devices. It has been demonstrated that the monolayer PtSe₂ film possesses spin-layer locking²¹ with many interesting electronic properties.³² These intriguing properties suggest that PtSe₂ might be a promising candidate for investigating the SOT phenomenon. However, unlike other TMDs,¹⁷ the band structure of PtSe₂ does not show spin splitting. In addition, the type II Dirac cone appears much below the Fermi energy in the bulk PtSe₂.³⁰

In this work, we investigate SOT in PtSe₂/Ni₈₀Fe₂₀(or NiFe)/Pt heterostructures using the spin torque ferromagnetic resonance (STFMR) technique. We found a large increase in the effective damping constant (164%) in PtSe₂/NiFe/Pt compared to the NiFe/Pt control sample. Using angle-resolved STFMR measurements, we demonstrated that only conventional SOTs are generated in PtSe₂/NiFe/Pt, with spin polarization along the *y*-axis for a charge current flowing along the *x*-direction, which is in accordance with theoretical predictions.³³ From the line shape analysis, we determine an enhanced effective damping-like torque due to PtSe₂. We found a maximum interfacial charge-to-spin conversion efficiency of $-0.1 \pm 0.02 \text{ nm}^{-1}$ due to PtSe₂. Our band structure calculation of PtSe₂ that includes the proximity of the FM layer shows that NiFe introduces: (a) charge transfer from NiFe to PtSe₂, (b) a Rashba SOC due to the surface symmetry breaking, and (c) a proximity magnetic field induced spin-splitting that could lead to enhanced spin Hall conductivity (SHC) in the interface region. The enhanced SOT due to PtSe₂ is qualitatively explained using the substantial spin splitting introduced by the proximity magnetic field.

We used a thermally assisted conversion process to grow large-area PtSe₂ thin films.³⁴ HRTEM and XRD (section S1 in supplementary) measurements on PtSe₂ show the growth of crystalline films. Figure 1 (a) shows the cross-sectional HRTEM image of PtSe₂/NiFe/Pt stack. The image shows that the whole Pt layer gets selenized, and a high-quality PtSe₂ lattice with a 1T structure is formed. The

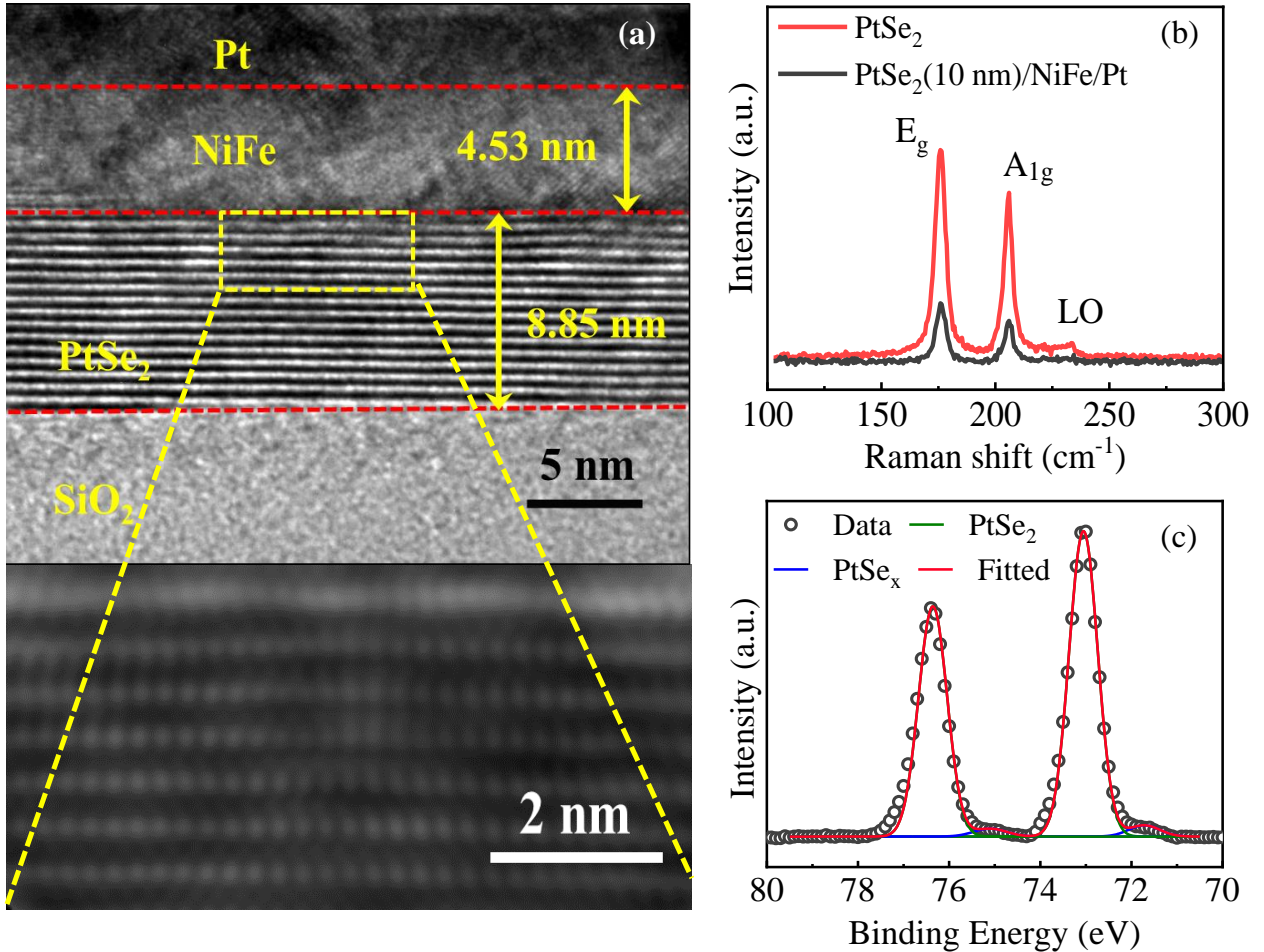


Figure 1: (a) cross-sectional HRTEM image of PtSe₂/NiFe/Pt stack. The interface is indicated by the red dashed lines. The magnified view of the square region is shown in the bottom part of the figure, showing the formation of high-quality PtSe₂ lattices (with 1T structure). (b) Raman spectra of PtSe₂ thin film (red curve) and that of the device after deposition of NiFe/Pt (black curve). The spectra show two strong peaks labeled as E_g and A_{1g} and one shoulder peak labeled as longitudinal optical (LO) mode. (c) X-ray photoelectron spectra of Pt-4f core level. Spectra were fitted with four peaks corresponding to PtSe₂ and PtSe_x. Splitting between doublets of Pt-4f peaks is found to be 3.3 eV.

thickness of PtSe₂ is found ≈ 9 nm, and the separation between two consecutive layers is ≈ 0.5 nm. Each layer corresponds to a monolayer of PtSe₂, which contains one Pt layer sandwiched between two Se layers. A magnified view of the square region is shown at the bottom of the figure. Based on HRTEM and AFM measurements (Section S1 in supplementary), we determine the thickness of PtSe₂ after selenization of 3 nm thick Pt to be (10 ± 1.0) nm. This increase in the thickness of Pt due to its selenization is well-known in the literature,³⁵ and it further confirms the complete selenization of the Pt layer. Figure 1 (b) shows the Raman spectra of PtSe₂, measured with a laser of wavelength 532 nm. The spectrum contains two distinct peaks that corresponds to PtSe₂: E_g at 176 cm⁻¹ and A_{1g} at 206 cm⁻¹. Here, the E_g corresponds to the in-plane vibrations of Se atoms moving away from each other while the A_{1g} corresponds to out-of-plane vibrations of Se atoms moving in the opposite directions.³⁶ A small peak labeled as longitudinal optical (LO) mode is also observed at 233 cm⁻¹, which is a combination of in-plane and out-of-plane vibrations of Pt and Se atoms.^{36,37} The position and intensity ratio of A_{1g} and E_g peaks confirm the presence of PtSe₂ in bulk form.³⁶ Similar spectra were obtained at multiple locations on the sample with a ratio of the intensity of A_{1g} and E_g peaks nearly identical (0.75 ± 0.02), confirming the formation of a large-area homogeneous thin film of PtSe₂. The chemical composition of PtSe₂ was verified further by X-ray photoelectron spectroscopy (XPS). Figure 1 (c) shows the Pt-4f core-level spectra. The binding energies of the different core levels have been calibrated using the C-1s peak and the core-level spectra have been best fitted with Gaussian profiles. Peaks corresponding to IV valency of Pt are observed at 76.3 and 73 eV, while peaks centered at 75.1 and 71.8 eV show the presence of PtSe_x phase in a small amount. The splitting between doublet for each phase is found to be 3.3 eV, consistent with literature.³⁸

Subsequently, we fabricated microstrip ($100 \times 40 \mu\text{m}^2$) devices for STFMR measurements using maskless lithography and lift-off method in two levels. To confirm the presence of PtSe₂ after deposition of NiFe/Pt and device fabrication, we perform Raman measurements [Fig. 1 (b)] by focusing the laser on the microstrip. The intensity ratio of A_{1g} and E_g was found to be similar compared to pure PtSe₂, indicating that the quality of PtSe₂ was not affected by the deposition of NiFe/Pt and our

fabrication steps. The overall reduction in the intensity of the peaks is due to the finite thickness of the top metal layers.

Figure 2 (a) depicts a schematic representation of the sample stack used for STFMR experiments, while Fig. 2 (b) shows the schematic of the STFMR circuit.¹¹ An amplitude-modulated radio frequency (RF) current, I_{RF} is applied to the device through the RF port of a bias-tee. The DC port of the bias-tee is used for both measuring the rectified mixing voltage using a lock-in amplifier and applying DC current. We vary the in-plane field angle, θ with respect to RF current, as defined in the zoomed-in image of Fig. 2 (b). Figure 2 (c) shows the measured anisotropic magnetoresistance

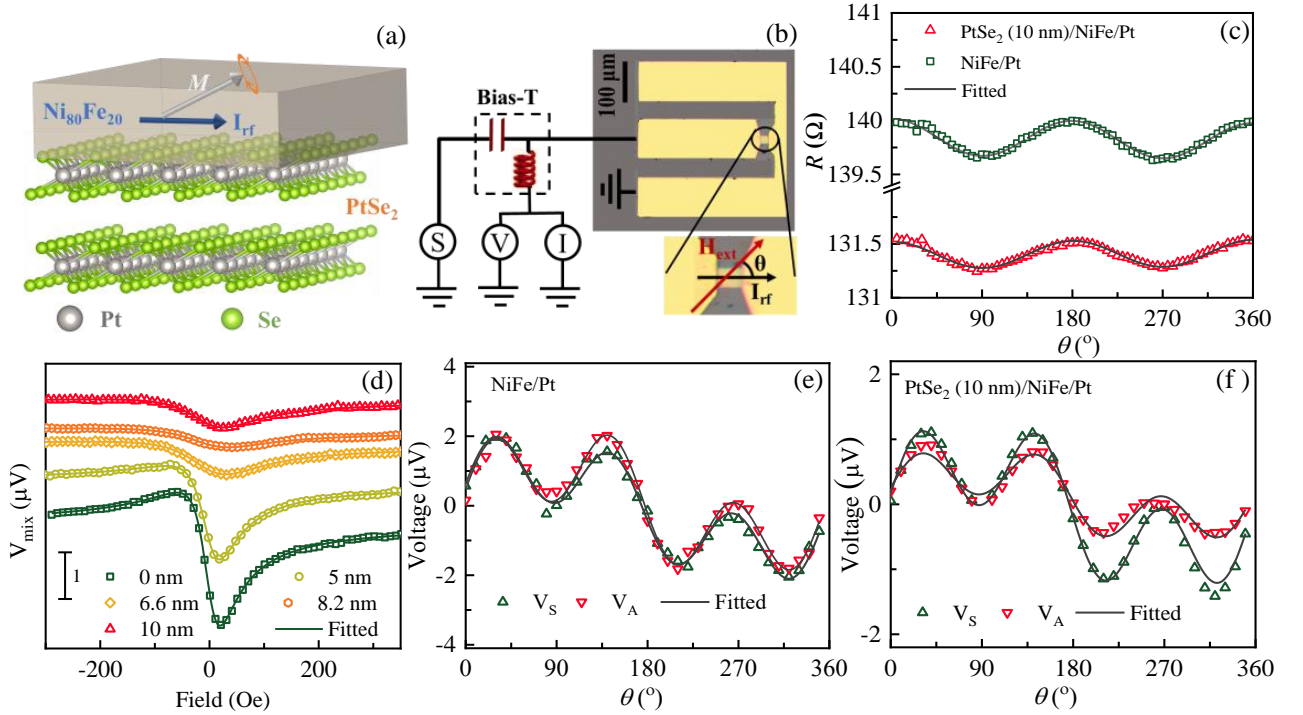


Figure 2: (a) Schematic of sample stack showing the direction of RF current and the precession of magnetization. (b) Schematic of STFMR set-up consisting of an optical image of the device. The directions of the RF current and applied field are also shown in the enlarged image. (c) Anisotropic magnetoresistance of PtSe₂ (10 nm)/NiFe (5 nm)/Pt (3 nm) to gather with control sample NiFe (5 nm)/Pt (3 nm). (d) Example of STFMR spectra measured at 5 GHz and $\theta = 50^\circ$ for PtSe₂(t)/NiFe/Pt for varying thickness of PtSe₂ layer. The plots are shifted for clarity. Angular dependence of V_S and V_A for (e) NiFe/Pt (f) PtSe₂ (10 nm)/NiFe/Pt, measured at 5 GHz. In all the plots, symbols represent the measured data, while solid lines represent fits as described in the main text.

(AMR) of PtSe₂ (10 nm)/NiFe (5 nm)/Pt (3 nm) to gather with control sample NiFe (5 nm)/Pt (3

nm). The solid lines are calculated AMR curve with $R = R_{\perp} + (R_{\parallel} - R_{\perp}) \cos^2 \theta$, where R_{\perp} denotes the resistance for $\theta = 90^\circ$ and R_{\parallel} denotes the resistance for $\theta = 0^\circ$. The percentage of AMR, *i.e.*, $(R_{\parallel} - R_{\perp})/R_{\perp}$ is found to be 0.19% for PtSe₂/NiFe/Pt and 0.24% for NiFe/Pt. Using a parallel resistor model, we estimate that the resistance of PtSe₂ to be $\approx 2 \text{ k}\Omega$ and the resistivity to be $\approx 1955 \mu\Omega \text{ cm}$. Figure 2 (d) shows the STFMR spectra for PtSe₂/NiFe/Pt to gather with the control sample NiFe/Pt measured at 5 GHz with a magnetic field applied at an angle of $\theta = 50^\circ$ for various thickness of PtSe₂. The data for other frequencies can be found in supplementary Sec. S2. The line-shape of STFMR spectra for PtSe₂/NiFe/Pt is found to be more symmetric compared to the control sample. The measured STFMR spectra can be fitted using the following equation:^{4,11}

$$V_{\text{mix}} = V_{\text{S}} \frac{\Delta H^2}{\Delta H^2 + (H - H_{\text{r}})^2} + V_{\text{A}} \frac{\Delta H(H - H_{\text{r}})}{\Delta H^2 + (H - H_{\text{r}})^2} \quad (1)$$

where, H is the applied magnetic field, ΔH is the linewidth, H_{r} is the resonance field, and V_{S} and V_{A} are the amplitudes of the symmetric and antisymmetric voltage components, respectively. By fitting the measured V_{mix} with above equation, we determine ΔH , H_{r} , V_{S} and V_{A} . First, we performed angular-dependent STFMR measurements to determine the spin polarization of the interface-generated spin current. The angular dependence of V_{S} and V_{A} is depicted in Fig. 2 (e) and (f) for NiFe/Pt and PtSe₂(10 nm)/NiFe/Pt respectively, which follows the conventional $\sin 2\theta \cos \theta$ dependence (solid lines), showing that the spin-polarization is along y -axis, for a charge current along the x -axis, which is similar to Pt and other heavy metals.^{4,23} Next, we determine the Gilbert damping constant, α by fitting the ΔH versus frequency data [Fig. 3 (a)] using:^{4,11}

$$\Delta H = \frac{2\pi\alpha}{\gamma} f + \Delta H_0 \quad (2)$$

Here, γ is the gyromagnetic ratio, and ΔH_0 is inhomogeneous linewidth which depends on magnetic inhomogeneity. The extracted value of α was plotted with the thickness of PtSe₂ (d_{PtSe_2}) in the *inset* of Fig. 3 (a). The value of α increases and becomes nearly constant for $d_{\text{PtSe}_2} \geq 6.5 \text{ nm}$. The

average value of α for $d_{\text{PtSe}_2} \geq 6.5$ nm is (0.045 ± 0.007) , which is 165% higher than the control sample. From this, we determine spin mixing conductance to be $\approx 7.6 \times 10^{19} \text{m}^{-2}$, which is higher than other TMD/NiFe systems.^{16,17} The inhomogeneous linewidth, ΔH_0 is found to be similar for all the devices $\approx (5 \pm 3)$ Oe, indicating no significant degradation in the quality of magnetic layer (NiFe) grown on PtSe₂. Furthermore, the linear behavior of linewidth with frequency indicates the absence of two-magnon scattering.³⁹ We calculate M_{eff} for different stacks by fitting the behavior of the frequency *versus* resonance field [Fig. 3 (b)] with the Kittel formula:

$$f = \frac{\gamma}{2\pi} \sqrt{(H_r + H_k)(H_r + H_k + 4\pi M_{\text{eff}})} \quad (3)$$

Here, H_k and M_{eff} are the anisotropy field and effective magnetization of the FM layer, respectively. By fitting the experimental data with the above equation, we found $4\pi M_{\text{eff}}$ decreases with the thickness of PtSe₂ as shown in the *inset* of Fig. 3(b). The effective magnetization $4\pi M_{\text{eff}}$ is given by $4\pi M_{\text{eff}} = 4\pi M_s - 2K_s/M_s t_{\text{NiFe}}$, where K_s is the surface anisotropy constant, t_{NiFe} is the thickness of the FM layer, and M_s is the saturation magnetization. Since K_s is proportional to interfacial spin-orbit coupling, we believe the decrease of M_{eff} for PtSe₂/NiFe/Pt is caused by the increase in interfacial spin-orbit coupling due to d - d hybridization, similar to previous reports for other TMD/FM systems.^{40,41}

As stated previously, PtSe₂ has a resistance greater than $2 \text{ k}\Omega$; therefore, the current flowing through the PtSe₂ layer is only 6% of the total current. Consequently, we anticipate SOT arising from (i) the interface between PtSe₂ and NiFe and (ii) the spin Hall effect of the Pt capping. Here, we neglect self-induced torque in NiFe, which is normally one order of magnitude lower.⁴² In order to quantify charge-to-spin conversion due to PtSe₂, we have used line shape analysis. In this method, the SOT efficiency, ξ_{SOT} is expressed as:⁴

$$\xi_{\text{SOT}} = \frac{V_S}{V_A} \frac{e\mu_0 M_s t_{\text{NiFe}} d}{\hbar} \sqrt{1 + \frac{4\pi M_{\text{eff}}}{H_r}} \quad (4)$$

Here, e is the electronic charge, and \hbar is the reduced Planck's constant. Here, d is the thickness of the non-magnetic layer. The above expression is valid when the field-like torque is negligible. In our case, we determined field-like torque from the anti-symmetric component of V_{mix} as discussed in the supplementary Sec. S4. We found field-like torque to be negligible for both NiFe/Pt and PtSe₂/NiFe/Pt. However, the above equation is normally used for the case of FM/NM bilayer samples. For the trilayer system of PtSe₂/NiFe/Pt, the lineshape method represents an *effective* spin-orbit torque efficiency, $\xi_{\text{SOT}}^{\text{eff}}$.⁴³ Since the conductivity of PtSe₂, is much lower than that of Pt, we assume that the Oersted field is only due to the Pt layer. With these assumptions, we determine $\xi_{\text{SOT}}^{\text{eff}}$, which includes the contribution of the top Pt layer and the interfacial contribution of PtSe₂. For this case, we use the thickness of Pt for d in Eq. 4.⁴³ In Fig 3 (c), the value of $\xi_{\text{SOT}}^{\text{eff}}$ has been plotted with frequency. The average value of $\xi_{\text{SOT}}^{\text{eff}}$ was further calculated and plotted in Fig. 3 (d) for different thicknesses of PtSe₂. The value of $\xi_{\text{SOT}}^{\text{eff}}$ for $d_{\text{PtSe}_2} \approx 5$ nm, was found to be very close to the control sample, but it increases upto $(50 \pm 13)\%$ for higher thickness. The value of $\xi_{\text{SOT}}^{\text{eff}}$ is constant with $d_{\text{PtSe}_2} > 5$ nm. We also performed dc Planar Hall effect measurements by fabricating Hall bars. These measurements also show a similar increase of damping-like torque as discussed in supplementary material Sec. S5. The increase of $\xi_{\text{SOT}}^{\text{eff}}$ due to the presence of PtSe₂ indicates that the sign of spin current due to PtSe₂ is opposite to that of the Pt layer. In order to extract the contribution of PtSe₂, we use the symmetric and asymmetric part of the V_{mix} of the control sample (see supplementary Sec. S3), which also eliminates SOT from the Pt cap layer [mechanisms (ii) mentioned above]. Considering the interfacial effect as the origin of SOT, we extract the interfacial charge-to-spin conversion (q_{ICS}) following Kondou *et al.*⁴⁴ Here, q_{ICS} is defined as 3D spin current (J_s) per unit 2D charge current (j_c). The maximum interfacial charge-to-spin conversion due to PtSe₂ ($q_{\text{ICS}}^{\text{PtSe}_2}$) is determined to be -0.1 nm^{-1} . For the control samples, the interfacial charge-to-spin conversion is 0.03 nm^{-1} . Thus the magnitude of interfacial charge-to-spin conversion is nearly three times larger compared to Pt. q_{ICS} of PtSe₂ is also higher compared to that of PtTe₂.²⁹ In this reference, the authors reported spin Hall angle/damping-like torque. Since we report an interfacial damping-like SOT, the efficiency of

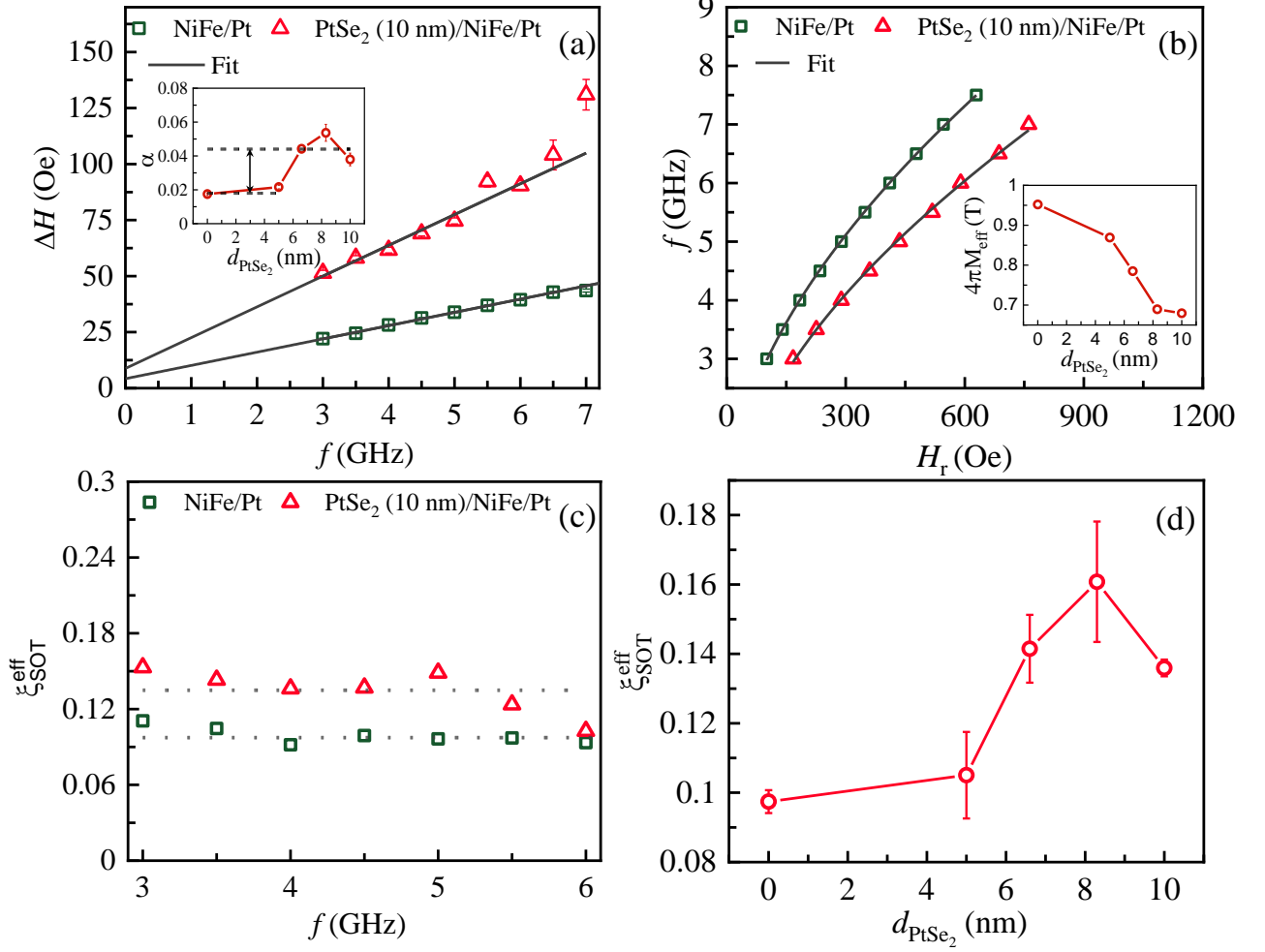


Figure 3: (a) The linewidth versus frequency for NiFe/Pt and PtSe₂(10 nm)/NiFe/Pt. The inset shows a variation of the Gilbert damping parameter (α) with the thickness of PtSe₂ (d_{PtSe_2}) in the PtSe₂/NiFe/Pt stack. The dashed line in the inset shows the average value of α for $d_{\text{PtSe}_2} \geq 6.5$ nm. (b) Resonance field versus frequency for NiFe/Pt and PtSe₂(10 nm)/NiFe/Pt. The inset shows the variation of effective magnetization (M_{eff}) with d_{PtSe_2} . (c) Variation of effective SOT efficiency with frequency for PtSe₂(10)/NiFe/Pt and NiFe/Pt. The dotted lines represent the average values. (d) Variation of effective SOT efficiency, $\xi_{\text{SOT}}^{\text{eff}}$ with d_{PtSe_2} . Each data point represents the average of three devices.

PtTe₂-work needs to be divided by the thickness of PtTe₂ for comparison with our work. Accordingly, the q_{ICS} of PtTe₂-work is $0.003 - 0.033 \text{ nm}^{-1}$, which is lower than our study. q_{ICS} value for PtSe₂ is also found to be higher compared to W, ($q_{\text{ICS}} = 0.06 \text{ nm}^{-1}$)⁴⁵ Bi₂Te₃, ($q_{\text{ICS}} = 0.05 \text{ nm}^{-1}$)⁴⁵ and PtTe₂ ($q_{\text{ICS}} = 0.003 - 0.033 \text{ nm}^{-1}$)²⁹ but it is lower than sputtered Bi_{*x*}Se_{1-*x*} thin films⁴⁶ and comparable to Ta ($q_{\text{ICS}} = 0.1 \text{ nm}^{-1}$).⁴⁵

The spin degeneracy in bulk PtSe₂ band structure is protected due to the presence of both inversion and time-reversal symmetries.²¹ Hence, the Rashba-Edelstein effect can be ruled out as the cause of SOT. In such cases, the origin of SOT by the interface is not very clear. Another possibility is that NiFe at the interface with PtSe₂ is playing a crucial role in generating SOT. In order to understand the mechanism in detail, we have performed a series of ab-initio calculations using density-functional theory (DFT). The results show that NiFe introduces three things: (a) Charge transfer from NiFe to PtSe₂, (b) A Rashba SOC due to the surface symmetry breaking, and (c) A proximity magnetic field that could lead to enhanced SHC in the interface region.

Monolayer PtSe₂ is semi-conducting, and the gap closes for (PtSe₂)_{*n*}, when the number of monolayers $n \geq 4$, with the band structure tending towards that of the bulk, with electron and hole pockets as indicated in Fig. 4 (a). In the (PtSe₂)₆/NiFe in Fig. 4 (b), we can clearly identify the bulk-like PtSe₂ bands intermixed with the NiFe bands running around the gap region. We find a significant electron transfer to the interface PtSe₂ layers from NiFe ($\sim 0.15 |e|$), consistent with the charge density difference contours shown in Fig. 4 (c), suggesting an enhanced conductivity as well as spin splitting of the PtSe₂ band structure near the interface.

A potential mechanism for spin accumulation is the Rashba-Edelstein effect (REE) due to the symmetry breaking at the interface. It is difficult to compute the Rashba SOC parameter α_R from the PtSe₂/NiFe calculations due to the intermixing of the NiFe bands. We have instead estimated it for the simpler case (PtSe₂)₄/Ni, where the four monolayers are enough to reproduce the bulk band structure, and a single Ni overlayer, representing NiFe, provides the symmetry breaking. For the top-most valence band at Γ , which represents the hole pocket in bulk PtSe₂, we find $\alpha_R \sim 0.01 \text{ eV}\cdot\text{\AA}$ (see

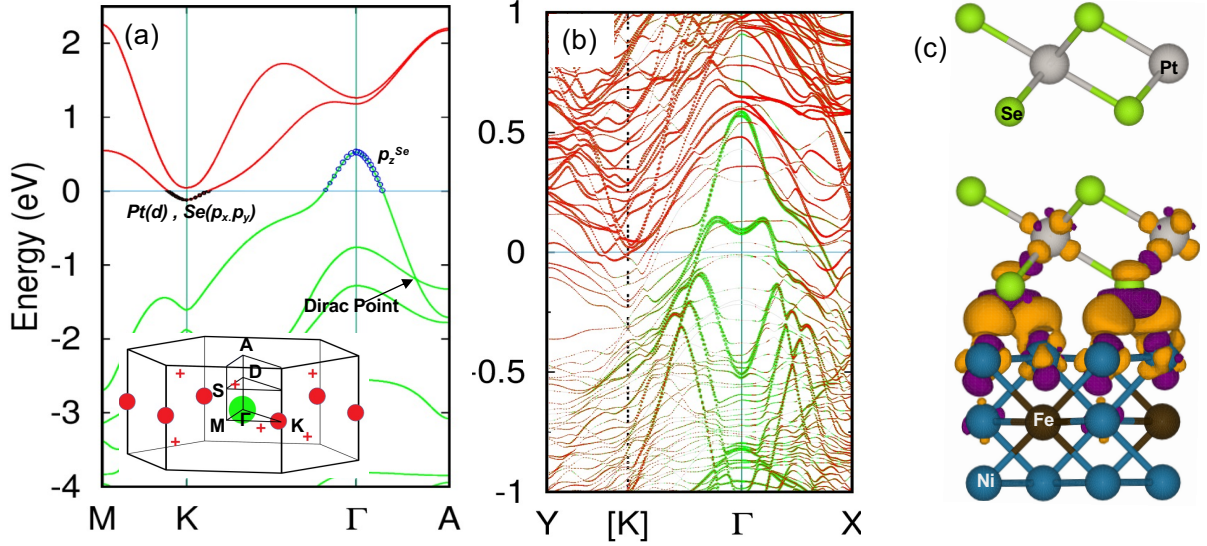


Figure 4: Density functional theory results for the PtSe₂/NiFe interface. (a) Band structure of bulk PtSe₂ indicating the electron pocket at K and the hole pocket at Γ at the Fermi energy $E_F = 0$, and the type-II Dirac cone at D, along the $\Gamma - A$ line. *Inset* shows the Brillouin zone, where the electron (green circle) and hole pockets (red circles and crosses) have been indicated. (b) Band structure of (PtSe₂)₆/NiFe showing the bulk-like bands of PtSe₂ (red for Pt and green for Se) with electron and hole pockets at Γ and K, interspersed with the NiFe bands (thin lines). The BZ in PtSe₂/NiFe is different from that of PtSe₂, but the Γ is the same, and the projection of the K point has been indicated by the square bracket. (c) Electron charge density difference contours indicating charge transfer from NiFe to the PtSe₂ interface layer, due to the interface formation. The orange and purple colors indicate, respectively, the charge accumulation and depletion regions.

Fig. S6 of supplementary materials), which is rather small. However, it has been estimated that PtSe₂ has a rather large momentum relaxation time $\tau \approx 80$ fs.⁴⁷ This leads to the Rashba-Edelstein length for the spin-charge conversion efficiency to be $\lambda_{RE} = j/j_s = \tau\alpha_R/\hbar \approx 1.2$ Å. This relatively low efficiency would be further reduced due to the proximity magnetic field, which tends to align the spin moments out of the plane, thereby reducing the REE. This suggests that the REE might play some role but is not a dominant mechanism for the spin accumulation at the interface. The type II Dirac cone in bulk PtSe₂ is also not expected to affect spin accumulation since it occurs well below the Fermi energy.

Due to the NiFe slab, the interface PtSe₂ layers will experience a proximity magnetic field, which could affect spin transport. Even though the PtSe₂ layers acquire very little magnetization ($0.03\mu_B$

for the first and $0.01\mu_B$ for the second layer PtSe₂, compared to $0.59\mu_B$ for Ni), there is a substantial spin-splitting of the PtSe₂ band structure due to the presence of NiFe. We have estimated this value to be $\Delta E \approx 0.10 - 0.15$ eV for the PtSe₂ states near E_F (see Fig. S7 of supplementary materials). This is significant and could lead to a large enhancement of the spin Hall conductivity (SHC). In fact, for the Pt/NiFe interface, earlier calculations by Kelly and coworkers⁴⁸ have revealed that the SHC for the Pt interface layers adjacent to the NiFe is enhanced by a factor of approximately twenty-five as compared to the Pt bulk layers. This suggests that the proximity magnetic field in the interfacial PtSe₂ plays an important role in the strong spin-charge conversion observed in the samples.

In conclusion, we demonstrated efficient charge-to-spin conversion in PtSe₂/NiFe/Pt using scalable large-area thin films of PtSe₂. Our findings indicate that the interface between PtSe₂ and NiFe can generate a significant current-induced damping-like torque. The corresponding *interfacial* charge-to-spin conversion efficiency is -0.1 ± 0.02 nm⁻¹, which is three times that of the control sample NiFe/Pt as well as PtTe₂.²⁹ Our band structure calculations suggest that the proximity magnetic field in the interfacial PtSe₂ plays an essential role in the strong charge-to-spin conversion observed in our samples. Our work demonstrates a novel form of SOT to obtain high charge-to-spin conversion efficiencies for device applications. Additionally, our work demonstrates that "SOT through a proximity magnetic field" needs to be considered for explaining SOT observed in other TMD-based material systems.

Methods

Large-area PtSe₂ thin films were grown using thermally assisted conversion process.³⁴ First, a 3-nm-thick Pt layer was deposited on a Si/SiO₂ substrate using magnetron sputtering. The base pressure of the sputter deposition system was better than 5×10^{-8} Torr. The sample was then transferred to a two-zone furnace for the selenization process. The substrate with the pre-deposited Pt layer was maintained at 500 °C, while the Se precursors were maintained at 280 °C. N₂ gas was used as a carrier

gas to direct Se species toward the substrate. By optimizing the substrate temperature, we found that the thermally assisted conversion of Pt into PtSe₂ takes place at a substrate temperature of 500 °C.³⁴

Structural characterization of PtSe₂ was done using cross-sectional HRTEM, XRD, Raman spectroscopy, XPS and AFM. The HRTEM measurements were performed on an FEI, TECNAI G2 F30, and ST microscope with an accelerating voltage 300 kV. XRD of PtSe₂ film was measured in $\theta - 2\theta$ mode, where X-rays of Cu-K _{α} line having a wavelength of 1.54 Å were used. Raman spectra of PtSe₂ were measured with a laser of wavelength 532 nm. XPS was recorded using AXIS Supra with the monochromatic Al-K _{α} X-ray source (1486.6 eV). The thickness of thin films was measured using AFM.

Subsequently, we fabricated microstrip ($100 \times 40 \mu\text{m}^2$) devices for STFMR measurements using a lift-off method in two levels. In the first level, a 3-nm-thick Pt layer was deposited on the patterned area and was later selenized following the method discussed above. Using magnetron sputtering, a NiFe (5 nm)/Pt (3 nm), bilayer was subsequently deposited. In the second level, co-planar waveguides were fabricated using optical lithography and lift-off from Au(80 nm)/Cr(10 nm).

Acknowledgement

The partial support from the Science & Engineering research board (SERB File no. CRG/2018/001012), the Ministry of Human Resource Development under the IMPRINT program (Grant no: 7519 and 7058), the Department of Electronics and Information Technology (DeitY), Joint Advanced Technology Centre at IIT Delhi, and the Grand Challenge project supported by IIT Delhi are gratefully acknowledged. Richa gratefully acknowledges the financial support from the Council of Scientific and Industrial Research (CSIR), Government of India. Theory work including the DFT calculations is funded by the Department of Science and Technology, India, through Grant No. CRG/2020/004330. SS thanks the United States-India Educational Foundation (USIEF) for their support through a Fulbright-Nehru Fellowship, jointly funded by the Governments of the United States and India. BRKN acknowl-

edges the support of HPCE, IIT Madras for providing computational facilities.

AUTHOR DECLARATIONS

Conflict of Interest

The authors have no conflicts to disclose.

DATA AVAILABILITY

The data that support the findings of this study are available from the corresponding author upon reasonable request.

References

- (1) Manchon, A.; Železný, J.; Miron, I. M.; Jungwirth, T.; Sinova, J.; Thiaville, A.; Garello, K.; Gambardella, P. Current-induced spin-orbit torques in ferromagnetic and antiferromagnetic systems. *Rev. Mod. Phys.* **2019**, *91*, 035004.
- (2) Dyakonov, M. I.; Perel, V. Current-induced spin orientation of electrons in semiconductors. *Phys. Lett. A* **1971**, *35*, 459–460.
- (3) Bychkov, Y. A. Properties of 2D electron gas with lifted spectral degeneracy. *JETP Lett.* **1984**, *39*, 78–81.
- (4) Liu, L.; Moriyama, T.; Ralph, D.; Buhrman, R. Spin-torque ferromagnetic resonance induced by the spin Hall effect. *Phys. Rev. Lett.* **2011**, *106*, 036601.
- (5) Skowroński, W.; Karwacki, Ł.; Zietek, S.; Kanak, J.; Łazarski, S.; Grochot, K.; Stobiecki, T.; Kuświk, P.; Stobiecki, F.; Barnaś, J. Determination of Spin Hall Angle in Heavy-Metal/Co -

- Fe -B -Based Heterostructures with Interfacial Spin-Orbit Fields. *Phys. Rev. Appl.* **2019**, *11*, 024039.
- (6) Pai, C.-F.; Liu, L.; Li, Y.; Tseng, H.; Ralph, D.; Buhrman, R. Spin transfer torque devices utilizing the giant spin Hall effect of tungsten. *Appl. Phys. Lett.* **2012**, *101*, 122404.
- (7) Bansal, R.; Nirala, G.; Kumar, A.; Chaudhary, S.; Muduli, P. Large spin hall angle in β -W thin films grown on CoFeB without oxygen plasma. *Spin* **2018**, *8*, 1850018.
- (8) Liu, L.; Pai, C.-F.; Li, Y.; Tseng, H.; Ralph, D.; Buhrman, R. Spin-torque switching with the giant spin Hall effect of tantalum. *Science* **2012**, *336*, 555–558.
- (9) Kumar, A.; Bansal, R.; Chaudhary, S.; Muduli, P. K. Large spin current generation by the spin Hall effect in mixed crystalline phase Ta thin films. *Phys. Rev. B* **2018**, *98*, 104403.
- (10) Demasius, K.-U.; Phung, T.; Zhang, W.; Hughes, B. P.; Yang, S.-H.; Kellock, A.; Han, W.; Pushp, A.; Parkin, S. S. Enhanced spin-orbit torques by oxygen incorporation in tungsten films. *Nat. Commun.* **2016**, *7*, 10644.
- (11) Kumar, A.; Sharma, R.; Ali Khan, K. I.; Murapaka, C.; Lim, G. J.; Lew, W. S.; Chaudhary, S.; Muduli, P. K. Large damping-like spin-orbit torque and improved device performance utilizing mixed-phase Ta. *ACS Appl. Electron. Mater.* **2021**, *3*, 3139–3146.
- (12) Behera, N.; Fulara, H.; Bainsla, L.; Kumar, A.; Zahedinejad, M.; Houshang, A.; Åkerman, J. Energy-Efficient $W_{100-x}Ta_x/Co-Fe-B/MgO$ Spin Hall Nano-Oscillators. *Phys. Rev. Appl.* **2022**, *18*, 024017.
- (13) Chen, R.-S.; Tang, C.-C.; Shen, W.-C.; Huang, Y.-S. Thickness-dependent electrical conductivities and ohmic contacts in transition metal dichalcogenides multilayers. *Nanotechnology* **2014**, *25*, 415706.

- (14) Behera, R. K.; Mishra, L.; Panigrahi, A.; Sahoo, P. K.; Sarangi, M. K. Tunable Conductance of MoS₂ and WS₂ Quantum Dots by Electron Transfer with Redox-Active Quinone. *ACS Appl. Mater. Interfaces* **2022**, *14*, 5750–5761.
- (15) Zhu, Z. Y.; Cheng, Y. C.; Schwingenschlögl, U. Giant spin-orbit-induced spin splitting in two-dimensional transition-metal dichalcogenide semiconductors. *Phys. Rev. B* **2011**, *84*, 153402.
- (16) Bansal, R.; Kumar, A.; Chowdhury, N.; Sisodia, N.; Barvat, A.; Dogra, A.; Pal, P.; Muduli, P. Extrinsic spin-orbit coupling induced enhanced spin pumping in few-layer MoS₂/Py. *J. Magn. Mater.* **2019**, *476*, 337–341.
- (17) Bangar, H.; Kumar, A.; Chowdhury, N.; Mudgal, R.; Gupta, P.; Yadav, R. S.; Das, S.; Muduli, P. K. Large Spin-To-Charge Conversion at the Two-Dimensional Interface of Transition-Metal Dichalcogenides and Permalloy. *ACS Appl. Mater. Interfaces* **2022**, *14*, 41598–41604.
- (18) Kumar, A.; Chaurasiya, A. K.; Chowdhury, N.; Mondal, A. K.; Bansal, R.; Barvat, A.; Khanna, S. P.; Pal, P.; Chaudhary, S.; Barman, A.; Muduli, P. K. Direct measurement of interfacial Dzyaloshinskii–Moriya interaction at the MoS₂/Ni₈₀Fe₂₀ interface. *Appl. Phys. Lett.* **2020**, *116*, 232405.
- (19) Kang, M.; Kim, B.; Ryu, S. H.; Jung, S. W.; Kim, J.; Moreschini, L.; Jozwiak, C.; Rotenberg, E.; Bostwick, A.; Kim, K. S. Universal mechanism of band-gap engineering in transition-metal dichalcogenides. *Nano Lett.* **2017**, *17*, 1610–1615.
- (20) Nugera, F. A.; Sahoo, P. K.; Xin, Y.; Ambardar, S.; Voronine, D. V.; Kim, U. J.; Han, Y.; Son, H.; Gutiérrez, H. R. Bandgap engineering in 2D lateral heterostructures of transition metal dichalcogenides via controlled alloying. *Small* **2022**, *18*, 2106600.
- (21) Yao, W.; Wang, E.; Huang, H.; Deng, K.; Yan, M.; Zhang, K.; Miyamoto, K.; Okuda, T.; Li, L.; Wang, Y.; Gao, H.; Liu, C.; Duan, W.; Zhou, S. Direct observation of spin-layer locking by local Rashba effect in monolayer semiconducting PtSe₂ film. *Nat. Commun.* **2017**, *8*, 14216.

- (22) Liang, S.; Yang, H.; Renucci, P.; Tao, B.; Laczkowski, P.; Mc-Murtry, S.; Wang, G.; Marie, X.; George, J.-M.; Petit-Watelot, S.; Djéffal, A.; Mangin, S.; Jaffrès, H.; Lu, Y. Electrical spin injection and detection in molybdenum disulfide multilayer channel. *Nat. Commun.* **2017**, *8*, 14947.
- (23) MacNeill, D.; Stiehl, G.; Guimaraes, M.; Buhrman, R.; Park, J.; Ralph, D. Control of spin–orbit torques through crystal symmetry in WTe₂/ferromagnet bilayers. *Nat. Phys.* **2017**, *13*, 300–305.
- (24) Kao, I.; Muzzio, R.; Zhang, H.; Zhu, M.; Gobbo, J.; Yuan, S.; Weber, D.; Rao, R.; Li, J.; Edgar, J. H., et al. Deterministic switching of a perpendicularly polarized magnet using unconventional spin–orbit torques in WTe₂. *Nat. Mater.* **2022**, *21*, 1029–1034.
- (25) Zhao, B.; Karpiak, B.; Khokhriakov, D.; Johansson, A.; Hoque, A. M.; Xu, X.; Jiang, Y.; Mertig, I.; Dash, S. P. Unconventional charge–spin conversion in Weyl-semimetal WTe₂. *Adv. Mater.* **2020**, *32*, 2000818.
- (26) Lv, W.; Jia, Z.; Wang, B.; Lu, Y.; Luo, X.; Zhang, B.; Zeng, Z.; Liu, Z. Electric-field control of spin–orbit torques in WS₂/permalloy bilayers. *ACS Appl. Mater. Interfaces* **2018**, *10*, 2843–2849.
- (27) Zhao, Y.; Qiao, J.; Yu, Z.; Yu, P.; Xu, K.; Lau, S. P.; Zhou, W.; Liu, Z.; Wang, X.; Ji, W.; Chai, Y. High-electron-mobility and air-stable 2D layered PtSe₂ FETs. *Adv. Mater.* **2017**, *29*, 1604230.
- (28) Husain, S.; Gupta, R.; Kumar, A.; Kumar, P.; Behera, N.; Brucas, R.; Chaudhary, S.; Svedlindh, P. Emergence of spin–orbit torques in 2D transition metal dichalcogenides: A status update. *Appl. Phys. Rev.* **2020**, *7*, 041312.
- (29) Xu, H. et al. High spin hall conductivity in large-area type-II Dirac semimetal PtTe₂. *Adv. Mater.* **2020**, *32*, 2000513.

- (30) Zhang, K.; Yan, M.; Zhang, H.; Huang, H.; Arita, M.; Sun, Z.; Duan, W.; Wu, Y.; Zhou, S. Experimental evidence for type-II Dirac semimetal in PtSe₂. *Phys. Rev. B* **2017**, *96*, 125102.
- (31) Bahramy, M. et al. Ubiquitous formation of bulk Dirac cones and topological surface states from a single orbital manifold in transition-metal dichalcogenides. *Nat. Mater.* **2018**, *17*, 21–28.
- (32) Wang, Y. et al. Monolayer PtSe₂, a new semiconducting transition-metal-dichalcogenide, epitaxially grown by direct selenization of Pt. *Nano Lett.* **2015**, *15*, 4013–4018.
- (33) Liu, Y.; Shao, Q. Two-Dimensional Materials for Energy-Efficient Spin–Orbit Torque Devices. *ACS Nano* **2020**, *14*, 9389–9407.
- (34) Jakhar, A.; Kumar, P.; Moudgil, A.; Dhyani, V.; Das, S. Optically pumped broadband terahertz modulator based on nanostructured PtSe₂ thin films. *Adv. Opt. Mater.* **2020**, *8*, 1901714.
- (35) Yim, C.; Passi, V.; Lemme, M. C.; Duesberg, G. S.; Ó Coileáin, C.; Pallecchi, E.; Fadil, D.; McEvoy, N. Electrical devices from top-down structured platinum diselenide films. *NPJ 2D Mater. Appl.* **2018**, *2*, 5.
- (36) Yan, M. et al. High quality atomically thin PtSe₂ films grown by molecular beam epitaxy. *2D Mater.* **2017**, *4*, 045015.
- (37) Gulo, D. P.; Yeh, H.; Chang, W.-H.; Liu, H.-L. Temperature-dependent optical and vibrational properties of PtSe₂ thin films. *Sci. Rep.* **2020**, *10*, 19003.
- (38) Su, T.-Y.; Medina, H.; Chen, Y.-Z.; Wang, S.-W.; Lee, S.-S.; Shih, Y.-C.; Chen, C.-W.; Kuo, H.-C.; Chuang, F.-C.; Chueh, Y.-L. Phase-engineered PtSe₂-layered films by a plasma-assisted selenization process toward all PtSe₂-based field effect transistor to highly sensitive, flexible, and wide-spectrum photoresponse photodetectors. *Small* **2018**, *14*, 1800032.
- (39) Arias, R.; Mills, D. Extrinsic contributions to the ferromagnetic resonance response of ultrathin films. *Phys. Rev. B* **1999**, *60*, 7395.

- (40) Wu, G.; Ren, Y.; He, X.; Zhang, Y.; Xue, H.; Ji, Z.; Jin, Q.; Zhang, Z. Tuning Magnetization Dynamics with Strong Spin-Orbit Coupling in Transition-Metal Dichalcogenide/Co-Fe-B Heterostructures. *Phys. Rev. Appl.* **2020**, *13*, 024027.
- (41) Jamilpanah, L.; Hajiali, M.; Mohseni, S. M. Interfacial magnetic anisotropy in Py/MoS₂ bilayer. *J. Magn. Magn. Mater.* **2020**, *514*, 167206.
- (42) Fu, Q.; Liang, L.; Wang, W.; Yang, L.; Zhou, K.; Li, Z.; Yan, C.; Li, L.; Li, H.; Liu, R. Observation of nontrivial spin-orbit torque in single-layer ferromagnetic metals. *Phys. Rev. B* **2022**, *105*, 224417.
- (43) Liu, E.; Fache, T.; Cespedes-Berrocal, D.; Zhang, Z.; Petit-Watelot, S.; Mangin, S.; Xu, F.; Rojas-Sánchez, J.-C. Strain-enhanced charge-to-spin conversion in Ta/Fe/Pt multilayers grown on flexible mica substrate. *Phys. Rev. Appl.* **2019**, *12*, 044074.
- (44) Kondou, K.; Yoshimi, R.; Tsukazaki, A.; Fukuma, Y.; Matsuno, J.; Takahashi, K.; Kawasaki, M.; Tokura, Y.; Otani, Y. Fermi-level-dependent charge-to-spin current conversion by Dirac surface states of topological insulators. *Nat. Phys.* **2016**, *12*, 1027–1031.
- (45) Wu, H.; Zhang, P.; Deng, P.; Lan, Q.; Pan, Q.; Razavi, S. A.; Che, X.; Huang, L.; Dai, B.; Wong, K.; Han, X.; Wang, K. L. Room-temperature spin-orbit torque from topological surface states. *Phys. Rev. Lett.* **2019**, *123*, 207205.
- (46) Dc, M.; Grassi, R.; Chen, J.-Y.; Jamali, M.; Reifsnnyder Hickey, D.; Zhang, D.; Zhao, Z.; Li, H.; Quarterman, P.; Lv, Y., et al. Room-temperature high spin-orbit torque due to quantum confinement in sputtered Bi_xSe_(1-x) films. *Nat. Mater* **2018**, *17*, 800–807.
- (47) Kurpas, M.; Fabian, J. Intrinsic and extrinsic spin-orbit coupling and spin relaxation in monolayer PtSe₂. *Phys. Rev. B* **2021**, *103*, 125409.

- (48) Wang, L.; Wesselink, R.; Liu, Y.; Yuan, Z.; Xia, K.; Kelly, P. J. Giant room temperature interface spin Hall and inverse spin Hall effects. *Phys. Rev. Lett.* **2016**, *116*, 196602.